



BRIGHAM AND
WOMEN'S HOSPITAL

EPFL

SYSTEM INTEGRATION AND PRE-CLINICAL EVALUATION OF ADAPTIVE NEEDLE STEERING FOR IMAGE-GUIDED PROSTATE INTERVENTIONS

SURGICAL NAVIGATION AND ROBOTICS LABORATORY
Brigham and Women's Hospital and Harvard Medical School

Master Thesis

Supervisors:

Author:

Lisa MARESCHAL

Master student of Robotics

Prof. Nobuhiko HATA

Prof. Dimitri VAN DE
VILLE

Faculty of Microengineering
École Polytechnique Fédérale de Lausanne

April 2022

Contents

A Project context: motivation and related work	3
A.1 On the diagnosis of Prostate Cancer (PCa): towards targeted biopsy	3
A.2 On the treatment of PCa: towards targeted management	4
A.3 State-of-the-Art of needle guide devices for MR targeted biopsy	5
A.4 Unmet needs	5
A.5 Related work	6
B Paper section	9
1 Introduction	9
2 System Design	11
2.1 Communication architecture	11
2.2 Needle guide design and implementation	13
2.2.1 2-DOF guide	13
2.2.2 Depth and rotation measurements	15
2.2.3 Needle holder	16
2.2.4 Physician interface	16
3 Validation experiments	18
3.1 Integration assessment in virtual, semi-virtual and real hardware setups	18
3.2 Preliminary evaluation of adaptive compensation strategy	19
4 Results	20
4.1 Latency results in virtual, semi-virtual and real hardware setups	20
4.2 Preliminary accuracy results	21
5 Discussion	22
6 Conclusion	23
C Project Conclusion	24
D Annexes	26
D.1 Arduino connections diagram	26
D.2 Hardware Assembly Guide	27
E Supplementary experiments	29
E.1 Intermediate virtual testing	29
E.2 Testing in different gel phantom stiffness	30
E.3 Evaluation of the needle guide's settling time	31
E.4 Integration test with another sensorized needle method	31
REFERENCES	33

ACKNOWLEDGEMENTS

I would like to express my gratitude to Professor Nobuhiko Hata who gave me the opportunity to realize my thesis in the Surgical Navigation and Robotics laboratory (SNR), a Harvard Medical School-affiliated laboratory located in Brigham and Women's Hospital. Not only he dedicated time to help me achieve this project, but I also appreciated his teaching philosophy oriented on self-development which I will remember for life. I would also like to thank Professor Dimitri Van de Ville for his time and interest in supervising this thesis.

Thanks also to every member of the SNR laboratory and of the Laboratory for Computational Sensing and Robotics (John Hopkins's University) for sharing their expertise and constructive feedback. A particular thank to Mariana Bernardes, Pedro Moreira and Dimitri Lezcano who put a lot of effort to make system integration happen within the deadline of this thesis. I would also like to thank Ahmet Yildiz and Franklin King who assisted me with the 3D design and printing.

I would like to thank all of my friends, the ones who stayed in Switzerland and the ones met in Boston who made a 5930 km away place seem like home.

Last but not least, thank you to my parents and sister who supported me throughout the demanding studies of EPFL, this thesis is the fruit of all these years of love and support.

A Project context: motivation and related work

A.1 On the diagnosis of Prostate Cancer (PCa): towards targeted biopsy

Prostate cancer is one of the most common type of cancer and is responsible for a significant number of deaths among men [1],[2]. It is marked by uncontrolled growth of malignant cells in the prostate gland, an essential organ of male reproductive system. Most early-stage PCAs do not cause visible symptoms, making detection of the disease a core step to fight prostate cancer [3]. Usual screenings consist in serum prostate-specific antigen (PSA) tests [4] and digital rectal exams (DRE) [5]. PSA is a fast and non-invasive method to test for prostate diseases. However, multiple non-cancer-related factors can induce a high PSA level. As a consequence, an increasing number of prostate cancer are being diagnosed and treated even if some of them would have had no impact on the patient's life [6]. On the other hand, DRE often fails in detecting PCa [7]. These techniques are good screening methods but cannot establish by themselves a definitive diagnostic. When cancer is suspected, follow-up investigations involve PCa biopsies. The most commonly used prostate biopsy is transrectal ultrasound biopsy (TRUS-biopsy) where the clinician reaches the prostate using ultrasound feedback [8]. However, one can hardly distinguish prostate tumor from normal glandular tissue using ultrasound images. Thus, systemic biopsy that randomly samples the prostate often fails in detecting PCa (false-negative rate of up to 30% [9]). Transperineal prostate biopsy uses TRUS but the needle is inserted using a guide through the perineum. It is preferred as it tends to cause less complications [10]. In particular tumor location cases, it can also decrease the false negative rate but it still fails in detecting several prostate cancer. All these limitations motivate targeted biopsies rather than the conventional TRUS-biopsy. Targeted biopsies aim at guiding a needle towards the located tumor using high-resolution feedback from magnetic resonance imaging (MRI). Two MR-related techniques are explored for targeted biopsy: In-bore MR-guided biopsy and MR-fusion biopsy. In-bore MR-guided biopsy (Figure1) relies on real-time images acquired from MRI. MR-fusion biopsy (Figure2) uses a combination of diagnostic MRI taken before the intervention and real-time TRUS guidance to target specific points. An increasing number of study assessed the diagnostic accuracy of these multiparametric (mpMRI) biopsy methods ([11],[12],[13],[14],[15],[16]). According to a recent study [16], MRI-targeted biopsy detects more clinically significant cancer than the systematic biopsy (+12 percentage points) and less clinically insignificant cancer (-13 percentage points). These promising results encourage innovation in mpMRI for prostate diagnosis.

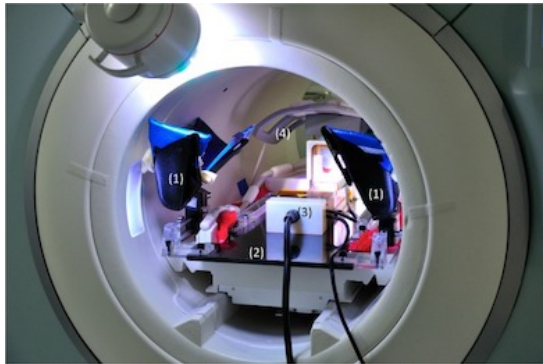


Figure 1: Interventional setup of a 3T MR-guided in-bore transperineal prostate biopsy 2014, Gaurie Tilak Bs et Al. It shows the (1) stirrups placed on (2) the patient table, (3) the robotic needle-guidance template, and (4) an abdominal surface coil, inside the MRI [17].



Figure 2: MR-fusion biopsy interface. On the top is shown the real-time ultrasound image acquired during operation. On the bottom is shown the pre-intervention MRI diagnostic image which locates the suspicious targeted region. This region is mapped onto the live US image. [18]

A.2 On the treatment of PCa: towards targeted management

PCa diagnostics determine a level of risk ranging from very low risk to very high risk using mainly the clinical stage, Gleason score (grade of the cancer cells stage) as well as PSA level [19]. A PCa of high risk requires a more drastic treatment than a PCa of low risk. Although in 33 % of cases the tumor percentage involvement represents less than 10 % of the prostate [20], the standard of primary care to this date is still heavy treatments. They are mainly prostatectomy which consists in removing the prostate and radiation therapy that aims at eliminating the cancerous cells by directing high energy rays towards the gland. An investigation study on ablated prostates revealed that a non-negligible number of the specimen did not contain a tumor [21], enlightening the possibility of wrong diagnosis. These common overdiagnosis induce numerous overtreatments and unnecessary risks for patients. For example, prostatectomy engenders for 30% of patients light incontinence that persists a long time after the operation [22]. Also, there is a risk of permanent erectile dysfunction or complications such as inguinal hernia [22]. Patients under radiation therapy usually undergo pain, fatigue and sleep disturbances [23]. Therefore, lighter treatments would alleviate the burden of radical prostate ablation.

Other management options exist for men diagnosed with prostate cancer. When radical treatments are not needed nor desired, the advised therapy is Active Surveillance (AS). This approach consists in regular check ups such as PSA, DRE or less frequently biopsies. If no new symptom nor abnormal result is observed, no treatment is given to the patient. AS reduces overtreatments and apparently does not compromise cancer-related survival at 10 years [24]. Nevertheless, repeated biopsy can also induce side-effects to the patient such as pain, irritations, blood etc. Also, even if without hard treatment the patient's life is not physically changing, AS often causes high levels of anxiety regarding the uncertainty of their cancer growing. On top of that, defining eligibility for AS is extremely difficult. The interest in focal treatment is growing as it destroys only the cancerous zone while avoiding surrounding sane tissues. Most of state-of-the-art therapies imply needle-shape

probes (for example radiation therapy, laser ablation, photodynamic therapy, cryoablation [25]) which would benefit from needle shape compensation discoveries.

A.3 State-of-the-Art of needle guide devices for MR targeted biopsy

As we have seen, the detection and ablation of prostate tumor gain in being targeted with better accuracy. To comply with strict requirements, people have developed needle guides solution. They mainly differ in the needle tracking, control algorithm and DOFs monitored and actuated. For example, a motorized needle guide template has been developed to automate needle placement in X-Z plane [26]. It eliminates human error that can be caused by miscommunication between the radiologist and the navigation operator or by miscounting the number of template holes. Nonetheless, there is no feedback and control on out-of-plane deviations due to in-body tissues. Gaurie Tilak et al measured a needle placement accuracy of 2.39 mm using in-bore transperineal prostate biopsy [17]. A more recent semi-autonomous PROST robot uses a two-joint arms system to correct trajectory. They achieved in a pre-clinical study an average error of 2.25 mm [27].

A.4 Unmet needs

As presented in the methods above, the placement of the needle is at the core of the success of PCa diagnosis and treatment. Targeted accuracy requirements are different for targeted biopsy and focal ablation. A study demonstrated that when the targeting error is below 3 mm, the performance of targeted biopsy is significantly better than the one of systematic biopsy. Focal ablation has even stricter requirements in order to cover the whole tumor while avoiding surrounding structures. An internal unpublished study assessed that with a placement error superior to 2.4 mm, the tumor coverage becomes less than 100%. In mpMRI techniques, the error variance is the sum of error variances for image registration and needle placement. Considering a registration error variance given by literature for MR-TRUS fusion of 1.8 mm, the maximal needle placement tolerated is 1.6 mm ($2.4^2 \text{mm} - 1.8^2 = x^2 \Rightarrow x^2 = 2.52 \Rightarrow x = 1.6$).

Currently, no existing needle placement techniques meet the presented requirements. Compensation strategy for the deviation have been explored such as model-based prediction or image-based tracking. However, obtaining the 3D position of the needle in real-time is challenging and these methods have not proven clinical feasibility. Plus, a compensation algorithm that relies on image tracking can only observe and correct deviation inside the body. Nevertheless, the leading cause of needle deviation usually happens at the skin entry and significantly impacts the accuracy that can be achieved.

While this accuracy requirement is unmet, prostate cancer detection and treatment remain heavily invasive with randomly sampled tissues and thoroughly ablated prostate. As mentioned earlier, this is a major concern since the introduction of PSA detects more and more low-level prostate cancer.

In order to address this need, an innovative method is proposed in this collaboration project. The solution relies on real-time sensing of the 3D needle shape during the insertion and immediate automated and manual correction. Implementation of this “closed-loop” adaptive needle guide would overcome the issues of false-negative biopsies and sub-optimal ablations.

A.5 Related work

This master's thesis is part of a project that extends over multiple years and multiple research teams. In order to have the context of the following development, it appears important to briefly explain the different parts of this project namely: the innovative sensorized needle, an improved control strategy, and an adaptive needle guide. A simplified architecture diagram is provided in Figure 3.

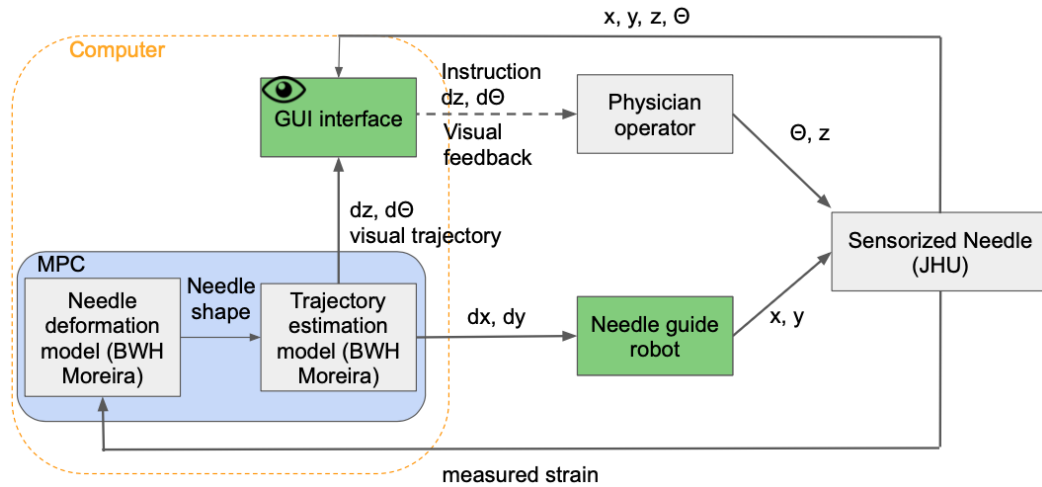


Figure 3: Architecture diagram of closed-loop control system. In green, the parts I was responsible for: the needle guide and GUI interface. In blue, the block diagram for the MPC strategy elaborated by a team at SNR lab. Lastly, the sensorized needle developed by collaborators at John Hopkins University (JHU).

- **A sensorized needle using fiber Bragg grating (FBG)**

Typical needle shape modelling rely on kinematics- or mechanical-based models but both make approximations that do not take into account the displacement of the needle tip inside the tissue in every direction. To overcome these limitations, image- or sensor-based techniques have been investigated and combine MRI, ultrasound and FBG. Although very accurate estimations of needle shapes have been achieved using FBG sensors (FBGs) (maximum error measured of 0.74 mm [28]), these techniques rely on 12 FBG sensors which reduce applicability. In this project, FBGs are explored because they have several advantages: they are bio-compatible and provide a better estimation of shape modelling with fewer approximations. An FBG sensor is a fiber-optic strain gauge that uses periodic refractive index to measure deformation. When the sensor is shrinked or extended, the wavelength moves in accordance to the strain.

In a preliminary unpublished study on FBG sensors performed by JHU members, the estimation model has demonstrated its ability to estimate needle shape deformation both in and out-of-plane. By adding the needle intrinsic curvature to the model, which reflects the effect on the environment on the needle curvature, the position of the tip should be estimated with an error smaller than 0.5 mm.

- **On-the-fly control algorithm**

Preliminary studies conducted in the laboratory suggested the solution of a multi-phase steering algorithm. This consists in using different mechanisms to steer the needle

depending on the phase of the needle insertion. Indeed, the experiments have demonstrated that the needle deviation can be decomposed into the pre-insertion phase and the post-insertion phase. The two types of deflections are elastic skin contact and tissue-needle interaction. The algorithm will correct the deviation according to the type of deviation that is observed.

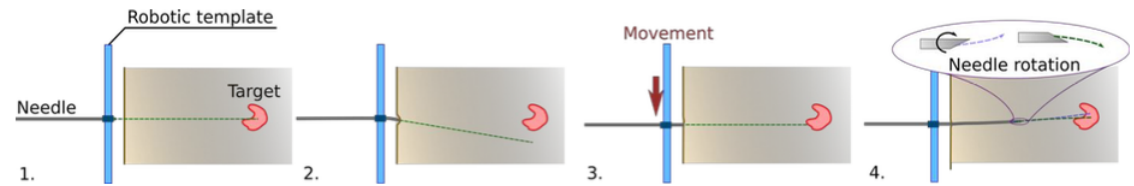


Figure 4: Proposed adaptive control strategy: 1. Alignment of robot with target point. 2. When elastic skin contact happens, 3. the correcting solution is to move the base of the needle guide using the two automated axis of the robot. 4. In case of tissue-needle deviation inside the body, instructions will be sent to the physician to rotate the needle so that the position of the tip cancels the observed deviation.

Thanks to that approach, the algorithm is simplified and only two robot-controlled axes are required instead of four.

The needle base control will be achieved thanks to a model predictive controller (MPC). It seems appropriate as the overall objective of MPC is to drive the output variables (i.e. the position parameters) to their optimal set points while preventing excessive movement of the input variable and maintaining variables within their specified constrained range. This is particularly important in clinically interventions as excessive movement can damage tissues. The output variables obtained by this model are the position parameters in x,y,z and θ . They are predicted using the needle shape model estimation provided by the FBGs.

- **Previous work on adaptive needle guide**

The overall strategy of the adaptive needle guide is to achieve a control of the needle base and tip to cancel deviation. To this end, a two degrees of freedom needle guide has been imagined to control the X and Z position. A previous team working on the project had 3D designed a first version of the needle guide. They also implemented a Gazebo simulation of the X and Z axes controlled by ROS2 nodes.

A solution had also been imagined to measure the rotation of the needle using an IMU that would rotate together with the needle. However, we decided not to follow with this solution as the double integration necessary to access position would also integrate twice the error and thus lack in precision.

- **Scope of my contribution**

The work presented in this thesis covers the system integration and the needle guide system. The system integration relies on ROS nodes which simplify the launching procedure and synchronization of the time frames of each part. Our hypothesis is that we can achieve integration with a latency of communication below 25 ms, which would allow a 10 times margin relative to the slowest component of the system.

It also consists in developing an adaptive needle to test the feasibility and accuracy of this innovative closed-loop system. The 2-DOF needle guide must align the needle with the desired skin entry point on the perineum. It must also provide a real-time measurement of the position and rotation along the insertion axis. Additionally, a needle holder has to be designed to satisfy the following requirements: hold a needle of multiple base sizes and comply with its sensing function.

A user interface also had to be implemented and communicate with ROS2 to fulfill the architecture system requirements. The implemented interface takes care of the calibration of the robot and provides real-time visual feedback to the user regarding the estimated needle shape, the actual position of the robot as well as the targeted position and orientation.

The system integration was validated through a set of experiments that imply latency and testing accuracy of the output control. As the control algorithm is not fully implemented yet, a simplified one is used and we aim at showing that the method can measure the success of the control.

The following paper section details the work accomplished in this thesis. Then, a project conclusion is provided. A supplementary experiments section presents other testing performed to bench-top the adaptive compensation method.

B Paper section

Abstract — Prostate cancer (PCa)’s false-negative diagnosis rate can be decreased using multiparametric magnetic resonance imaging biopsy (mpMRI-biopsy). One innovative approach is to separate the automated control of lateral/vertical axis and manual control of insertion and rotation. By using the 3D modeling of the needle shape and its base position, a model predictive control (MPC) can predict the ideal position of a needle guide and correct the trajectory in real-time. However, there is no existing integration system that allows testing of these developments. Thus, improved accuracy is not enabled and patients continue to suffer from over- and under-treatment. Our hypothesis is that the presented system can integrate (1) a sensorized needle, (2) a control algorithm, (3) a needle guide, and (4) a visual feedback interface, with a delay ten times faster than slower part of the system thus 25 ms. Our secondary hypothesis is that such system enables to test the compensation produced by the aforementioned technological breakthroughs. The proposed solution relies on Robotics Operating System 2 (ROS2) nodes and the Open Network Interface for Image-Guided Therapy (OpenIGTLINK) protocol. The needle guide features automated movement in lateral and vertical directions as well as sensing and manual movement of insertion and axial rotation. The integration has been validated by measuring the latency of information transfer both with simulation setup (mean of 6.9ms) and with physical hardware (mean of 9.4ms). This study enabled the first assessments of a novel sensing and control strategy for targeted prostate biopsy and provided a mean target error of 0.5 mm.

Index Terms — MR-targeted prostate biopsy, closed-loop control, needle guide, system integration, ROS2

1 Introduction

Prostate cancer accounts for 20% of newly diagnosed cancer in men population and ranks as a leading cause of death among them across the world [1], [2]. Since its introduction in the 1980s, the standard biopsy method for prostate cancer is transrectal ultrasound biopsy (TRUS-biopsy) [8]. In this method, tissues are sampled from 6 to 12 locations under ultrasound guidance without any information from diagnostic images. As a consequence, it

has a false-negative detection rate of up to 30% [9]. Alternatively, transperineal prostate biopsy uses TRUS but the needle is inserted with a guide through the perineum. This insertion method is preferred as it limits complications and yields better results when the tumor is located in difficult sites such as the anterior zone [29],[30]. However, as it uses longer needles, a deviation tends to occur and lead to important targeting error [10]. Additionally, with the vulgarization of PSA screenings comes an increased number of localized and early-stage prostate detected and treated. A study on prostatectomy specimen shows that since the introduction of PSA, it is less likely to find a tumor in extracted prostate [21]. This underlines the possibility of increasing number of overtreatments and unnecessary risks for several patients. Indeed, to this date, the standard of primary care for PCa is radical treatments acting on the entirety of the gland which induces side-effects such as incontinence and erectile dysfunction [22]. Therefore, there is a call for more accurate detection and focal treatment of prostate cancer. These limitations oriented research towards novel approaches that exploit MR-directed tissue sampling, known as targeted biopsy.

Recent discoveries have demonstrated that mpMRI provides an opportunity to significantly improve the localization and reachability of prostate tumor. Indeed, if the area of interest can be identified on high contrast MR images, the clinician can aim at sampling that region. Both in-bore and fusion MR-guided biopsy are explored. By relying on real-time images acquired from MRI, the in-bore method provides precise real-time feedback. It has proven to detect significant PCAs, especially in cases where a systemic biopsy would miss them [13]. This allows to reduce the number of cores thus limiting the side effects and complications. It does not rely on a second imaging modality (i.e. TRUS) thus removing registration error and permitting direct comparison of the needle location and target. However, this technique cannot be popularized yet because of the cost and limited availability of interventional MR equipment. MR-fusion biopsy targets suspicious points using diagnostic MRI taken before the intervention together with real-time TRUS guidance. It is highly promising because it uses the widely validated TRUS setup but with the advantage of increased resolution provided by MRI diagnostic images. Ahmed et al assessed the diagnostic accuracy of mpMRI and conventional TRUS-biopsy in PROstate MR Imaging Study (PROMIS) and revealed that mpMRI was more sensitive than TRUS-biopsy in detecting clinically significant PCa (93% vs 48%) [11], [12]. With targeted biopsy comes a strict placement accuracy that has been investigated in recent studies. A simulation has shown that when the placement error is reduced from 5 to 1 mm, cancer sensitivity increases from less than 0.35 to 0.7 [31]. Novel focal ablation treatments of PCa would also benefit from more accurate probes placement, which deviate similarly to biopsy needles. An internal unpublished study defined that a probe placement error of less than 1.6 mm is essential to reach 100% tumor coverage.

To reduce the targeting error, the commonly explored solution is the guidance of a needle. Gaurie Tilak et al measured a needle placement accuracy of 2.39 mm using in-bore transperineal prostate biopsy [17]. The recent semi-autonomous PROST robot pre-clinical validation provided an average error of 2.25 mm [27]. However, none of the existing needle guides meet the presented accuracy requirement. Indeed, typical methods try to correct the needle deviation inside the tissue but have no system to correct the deviation at the skin entry point. Nevertheless, the major trajectory deviation usually happens at the skin puncture. In order to address this issue, an innovative compensation method that takes into account environment-related parameters such as intrinsic curvature is proposed. It relies on two technological breakthroughs. First, a real-time sensing of the 3D needle shape during the insertion using a needle equipped with fiber Bragg grating (FBGs) sensors

along its length. Second, a multi-phase steering control algorithm decomposing the control strategy for elastic skin contact and tissue-needle interaction. However, there is no system integration and physical device allowing these developments to be tested in closed-loop, thus limiting correct detection and optimized ablation of PCa. In order to bring these developments from isolated innovations to clinically tested devices, connecting them is primordial. Successful system integration of these components is the first step towards implementation of this “closed-loop” adaptive guide that could overcome the issues of false-negative biopsies and sub-optimal ablations.

As we aim at achieving real-time control, the latency induced by communication should be minimized. No definition of real-time is globally agreed on in the research community. However, most clinically approved real-time system satisfy this requirement by examining the slowest part of their system. A typical rule of thumb inspired by signal reconstruction is to then to choose a securing factor of 10 and comply to that computed frequency [32]. In our case, the frequency of the Hyperion interrogator receiving curvature values is about 1kHz. Thus, we hypothesize that the limiting block to live application will not be the interrogator but the sensorized needle itself. The shape-sensing needle provides outputs with a frequency of approximately 4 Hz. As this frequency bounces a lot and according to the stated rule of thumb, we target a latency requirement below 25 ms ($4 * 10\text{Hz}$). As mentioned earlier, reaching a target error below 3 mm would have a significant impact on PCa biopsy results. Considering a registration error variance given by literature for MR-TRUS fusion of 1.8 mm, the needle placement goal of the final strategy is 2.4 mm. In this study, the sensorized needle is still in development and the controller does not take the trajectory shape, depth and rotation into account yet. Thus, this preliminary study provides first measures of such strategy to underline integration but cannot discriminate the feasibility and accuracy of the method.

2 System Design

2.1 Communication architecture

The system consists of a 3D real-time sensing of the needle deviation, a control algorithm that estimates ideal goal position and sends a corresponding instructions to the needle guide and to the user interface. On the following Figure 5, a global configuration diagram explains the responsibility of each sub-part. In order to bring together these sub-parts and have an easy-to-test system, every collaborator uses *ROS2 Foxy* as the software support and *Github* [33] as a sharing platform. This robotic operation system allows synchronous communication between parties as well as useful debugging tools to verify that every message is correctly sent and received. ROS2 was chosen over ROS because it allows to create fully distributed system, where each node is independent and not tight to a global master. This is the case in this project where each subsystem can be tested on its own but needs to be connected to the others for the final application. Another motivation for ROS2 is the coming end of life of ROS1 scheduled for 2025. The chosen release, ROS2 Foxy Fitzroy, was the latest one at the starting date of this project. An obstacle to integration is that every block of the system has several repositories, each using more than one launch files. This made the whole system impossible to test for any developer of one block. Another added complexity is that most of them contain different launch files for virtual and hardware implementation. To overcome these difficulties, a main repository named *System integration* aims at simplifying the testing process. First, this repository contains

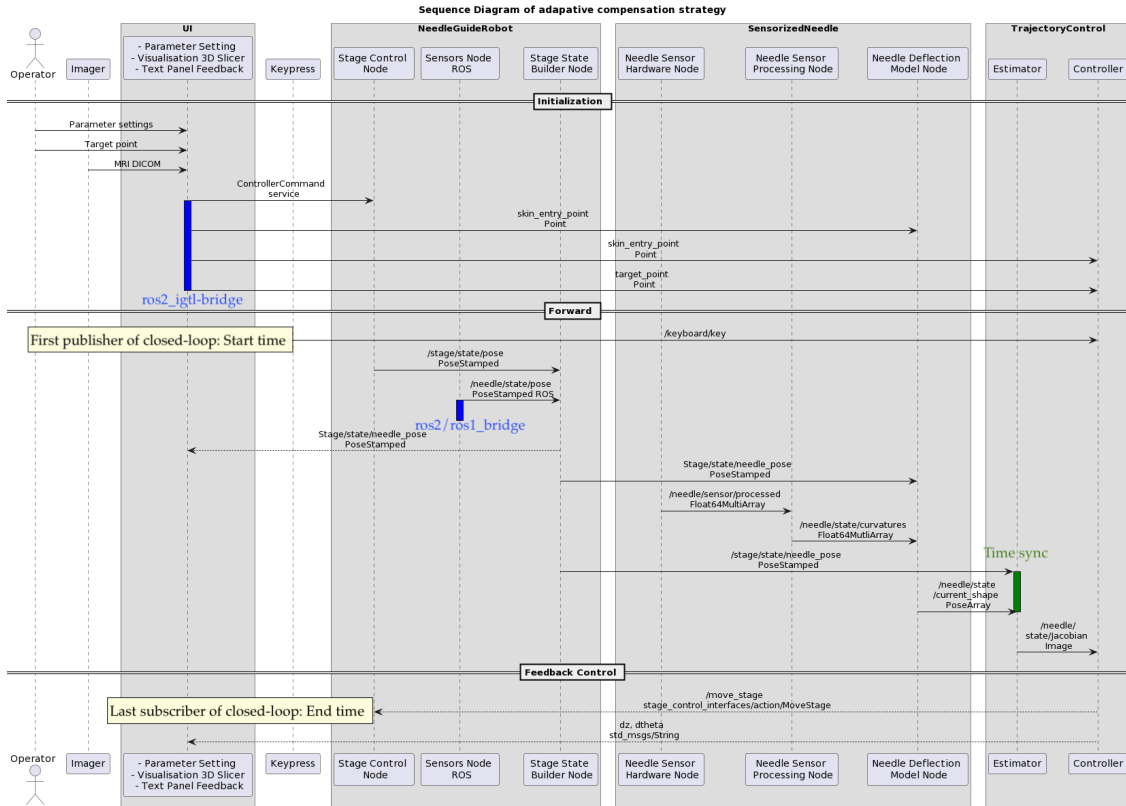


Figure 5: Sequence diagram of main nodes publishers and subscribers. Notes indicate the beginning and end publisher/subscriber used to define latency. Grey boxes highlight the different repositories.

detailed instructions on how to install and use the system. Second, it contains a global launch file that can launch every ROS2 node with its respective parameters with only one command. Thirdly, simulation level parameters have been added for each sub-part so that one can launch any combination of simulation and hardware level with the same command. Indeed, as collaborators are not in the same city/laboratory, this is a core step in the success of this project. Below are listed the different parameters with their corresponding simulation level.

- *sim_level* controls the Needle Guide Robot simulation level:
 - 0 : Emulated (dummy nodes) stage and sensors only
 - 1 : Virtual stage and sensors (Gazebo)
 - 2 : Physical stage and sensors
 - 3 : Both virtual and physical stages and physical sensors
- *sim_level_needle_sensing* controls the Shape-Sensing Needle Node simulation level:
 - 1 : Launches sensorized needle node demo
 - 2 : Launches node for the physical sensorized needle
- *sim_level_trajcontrol* for the Trajectory Control algorithm:
 - 1 : Launches control for system integration demo
 - 2 : Launches real control nodes

2.2 Needle guide design and implementation

To achieve full hardware integration, a needle guide providing movement and sensing of different degrees of freedom (DOF) required by the adaptive compensation strategy was implemented. Again, the approach combines two needle steering techniques: needle base control (X-Z) and needle tip control (rotation θ along insertion axis Y). The needle base control consists in shifting the needle holder along the skin surface to cancel out the bending of the needle due to the elastic skin contact. The needle tip tries to compensate for in-tissue deviation by giving counter-steering instructions to the physician. Thus, the needle base control requires automated movement in X and Z direction and must provide information of these positions. The needle tip control strategy requires the manual movement of the needle in the Y direction and manual rotation of the needle along its axis. It also has to provide the nodes with information of the actual depth and rotation position. The robot's kinematic configuration is shown schematically in Figure 6 and the needle base position equation in Figure 7. As we can see, a key point of this design is its simplicity coming from the decoupled method. This allows compatibility with previously developed and verified TRUS guidance setup and could make the implementation of such device to a clinical environment more fast-forward. The mechanical system has also been designed to reduce physical interference with TRUS and make it applicable to TRUS-guided operations. Table 1 summarizes the specifications of the proposed needle guide.

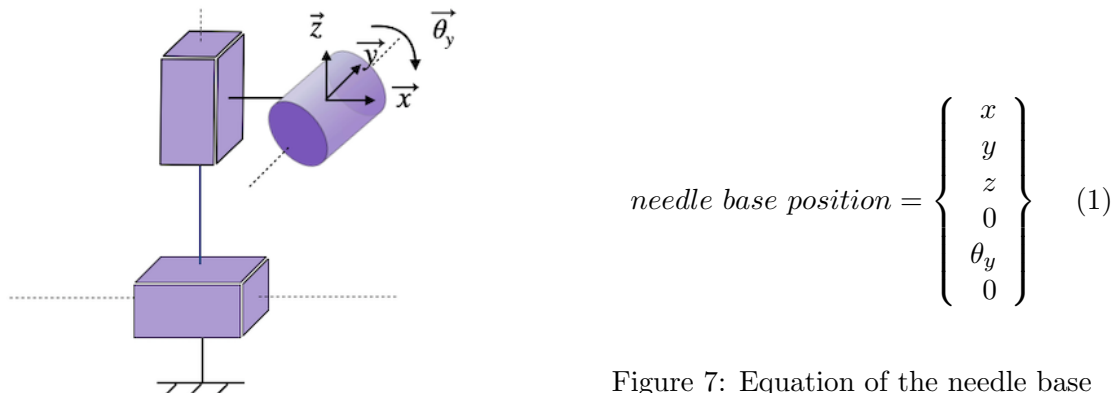


Figure 7: Equation of the needle base position.

Figure 6: Kinematic diagram of the needle guide.

According to the simple kinematics, the needle base position is directly defined by the x, y, z and θ values measured by the sensors as they all have the same reference axis. This reference frame is also the coordinate system of the whole architecture. Every node transforms its values to this reference frame.

2.2.1 2-DOF guide

The usual workspace for prostate biopsy cases is restricted due to the MRI setup. As the diameter of a scanner ranges from 60 cm to 70 cm, the interventional workspace left for the surgeon is limited and the perineal window is typically around 100 mm^2 [34]. The 2-DOF robot makes use of two perpendicular linear guides, the *Newmark's System Inc eTrack* linear stages (ET-100-11) which offer a travel length of 100 mm. The needle guide is thus covering a 100 cm^2 area which largely covers the scope of the prostate (around 35

Table 1: Design specifications of the proposed needle guide, provided by the chosen hardware.

Horizontal range [mm]	100
Vertical range [mm]	100
X-Z guide	automated
Y, θ guide	manual
Resolution X-Z [μm]	0.24
Resolution Y [mm]	1
Resolution θ [rad]	0.01

mm^2) and is reasonably small to fit inside an MRI. The stages are made of 6061 aluminum alloy and contain metallic parts. As a consequence, the robot presented here could not be used for in-bore testing as it would interfere with the scanner's electric and magnetic fields. Nonetheless, a similar setup could easily be reproduced to be MRI-compatible using more specific materials. At the stage of this study, the sensorized needle are not MRI-compatible and the goal is to test integration of the control and needles outside of the MR scanner.

As stated previously, the method's hypothesis is that the automated system will allow reaching the target with an overall accuracy of 2.4 mm. Considering that the measurement error of sensorized needle is inferior to 1.0 mm, a positioning accuracy inferior to 1.24 mm is targeted for the needle guide. By choosing linear guides with travel accuracy of 0.6 μm per mm of travel, we ensure that the limiting factor is not the linear guide's accuracy. The guides offer a resolution of 0.24 μm which allows to measure and control with negligible impact on the final target error.

In the context of validating the closed-loop control, the maximum speed that can be achieved should be able to compensate in real-time the deviation error computed by the MPC. Internal studies defined the success value for the settling time metric as a range from 0.5 to 1 second. The maximum deviation that could happen in one iteration should not be superior to 1mm as the clinician inserts the needle little by little. By approximating that the linear stages have to move of that same error distance in the opposite direction to correct the deviation, we can estimate that the required velocity is: $v = \frac{d}{t} = \frac{1}{0.5} = 2$ mm/s. A reasonable securing factor is 5. Thus, by choosing a linear guide of a speed of $2 * 5 = 10$ mm/s), we can assume that the linear stages should be able to achieve the correction fast enough. As the maximum speed that can be achieved by the *Newmarks*' guide is 25 mm/s, the needle guide should be able to comply such time range. Indeed, eTrack linear stages are specifically designed for applications requiring quick positioning of light payloads. The smaller lead screw option of 2 mm lead was sufficient to provide the above-mentioned requirements. A Newmark's Systems control study has measured the unidirectional repeatability of eTrack to be 10 μm thus the device is reliable which is crucial for clinical applications. The eTrack comes with a high torque size 17 stepper motor at the end of the travel distance. The linear stages are controlled by the NSC-2AL two axis stepper motor controller, also from *Newmark*. It is plugged to the stepper motor of both axis using a 9 pin connector that terminates the motor cables near the rear of the stage. The NSC-A2L is supplied with a +24 VDC power adapter. It also provides a USB interface for sending commands to the motors. The controller can drive the stepper motors for up to 1/8 of a step through micro-stepping. It utilizes a 32-bit microprocessor

to control the trajectory profile, acceleration, velocity, deceleration. Newmark provides an API in Python, C++, Visual basic, and Labview to programmatically control the motors. To integrate the control scheme to ROS2, we make use of their given C++ API for Linux, *Performax_Linux_Driver_104*, together with the *libusb-dev* library. The API was slightly outdated and required a few changes before being usable. The API provides functions to send and read information from the motor controller and acknowledges of good reception of the commands. This adds a safety layer to the communication protocol. The control of the physical linear guides uses the same organization than the control of the virtual linear stages. In a main parent package is the *adaptive_guide* package which has a launch file that starts the whole robot system up. Nodes from this package both operate movement of the linear stages when a control order is received and publish the position of the base in real-time.

2.2.2 Depth and rotation measurements

In order to provide the clinician with feedback during the operation as well as the necessary inputs of the deformation model and control algorithm, the depth and axial rotation have to be measured. For the depth, the simple solution of a sliding carriage over a linear potentiometer has been imagined. The chosen potentiometer from *Sofpot* is connected to an *Arduino Uno* board via a 3-pin connector. This linear position sensor is activated with a pressure of usually 1 to 3 N from the wiper. In our design, the wiper is a 3D printed plastic cylindrical part which accommodates an aluminium spring. The range of motion of the potentiometer is 150 mm and its reading has a 0.1 mm precision. Measuring axial rotation performed by the clinician is essential because it can have an important impact on the deviation of a bevel-tip needle and thus on the target error. The chosen solution consists in a rotary encoder that is attached to the 3D-printed sliding carriage and rotates together with the needle. The capacitive encoder is from *CUI Devices* and is an absolute, multi-turn, 14-bit encoder. With these specifications, the rotation can be measured with a 0.1 rad precision which corresponds roughly to the minimum step an experimented physician can achieve. It is also connected to the Arduino Uno board using RS-485 communication with a shielded twisted pair cable with a 6-pin connector. The rotary encoder clips to a mounting base which was fixed to the 3D-printed carriage part using 6 screws, allowing a good alignment. A CAD drawing of the sliding carriage assembled with the encoder base is provided in Figure 8. The sliding carriage is equipped with sleeve washers and we added greasing to improve the smoothness of the movement.

The Arduino Uno board is programmed using the Arduino IDE and values are read at a baud rate of 57600 bps. A challenge was to get real-time measurements sent via ROS2 to the deformation model node, the control algorithm node, and the interface node. However, no existing library allows sending information from Arduino Uno board to ROS2. A first implemented solution was to use an input output software to read values from port and save it to a file. Values were thus read from the Arduino port and saved to a file using Putty. Then, a ROS2 node published the last line of that file. In order to process information faster, both depth and rotation values were saved to the same file, separated by a semicolon. However, this solution adds a delay in the communication and we had to come up with an improved alternative. ROS has external plugins that have not been developed yet for ROS2 such as the rosserial library for Arduino boards. It allows to use the Arduino board as a ROS publisher/subscriber. A publisher was thus implemented to sense and publish the depth and rotation in ROS Noetic (latest release). Then, to make these values accessible from every ROS2 node, we make use of the ROS-ROS2 package which bridges the communication between ROS and ROS2 [35].

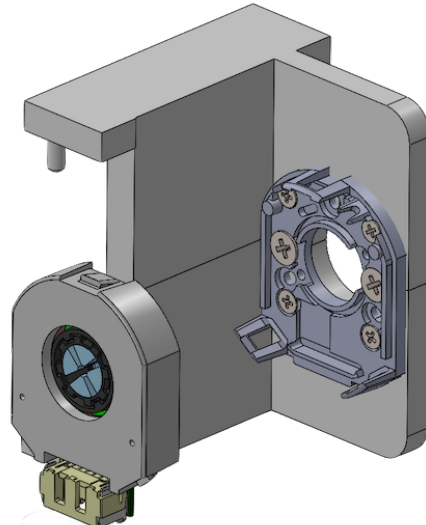


Figure 8: CAD drawing of the sliding carriage, with the encoder based attached, and the rotary encoder.

For the sake of virtual integration, the simulation code simply consists of a publisher that sends increasing values. The values range from -150 to 0 mm for the depth with an increment of 1mm and from 0 to 3.15 rad with an increment of 0.2 rad for the orientation. The publisher's topic is the same than with the hardware so one can test the exact same configuration than with the code for real hardware.

2.2.3 Needle holder

The needle holder has to comply to two principal requirements. One comes from the specifications of the sensorized needle and one from its sensing function. As sensorized needles of different gauges are being tested, they also come with different needle hubs (small part used by the physician to usually hold the needle). To fit with these different hubs shapes, a previously concept of holding is reused and adapted to attach to the rotary encoder. The imagined solution uses the smallest sleeve adapter provided by *CUI devices* of 2 mm \varnothing and a cross-shaped end that fits inside that adapter. This way, the needle holder provides the rotation information without any impact on the physician's side. Also, as mentioned above, the needle holder must allow insertion along the needle's axis (θ). To this end, the needle holder design is mounted on the presented sliding carriage. Finally, to facilitate mounting and 3D printing, the holder is parted in 3 pieces that can be assembled using screws (2.5mm \varnothing (x2)). A picture of the final needle holder is presented in Figure 9.

2.2.4 Physician interface

The GUI has both an initialization and feedback role. It was implemented in Python in 3D Slicer. A screenshot of the interface during an insertion can be seen in Figure 11.

The physician interface's first implemented feature is to establish connection between the GUI in 3D Slicer software and the ROS2 nodes of every party. This has been implemented using OpenIGTLink-ROS2 bridge [36]. This software has been chosen as it



Figure 9: Picture of the 3D printed needle holder. From left to right: the bottom cap, a central part adapted to different needle hubs and a top cap. The needle is secured to the sleeve adapter of CUI design thanks to its cross-end shape.

supports the import of tracking data sensors, it provides a simple solution to import real-time images from imaging scanner and facilitates integration of robot-assisted intervention systems. The interface is also in charge of the whole initialization phase of the protocol presented in Figure 10. It is responsible for setting and publishing the target point and skin entry position. For now, the default value for the skin entry point is to be perfectly aligned to the target point. However, one can manually enter other coordinates for the skin entry point. Future studies could use this functionality to explore if a slight angle relative to the target point can help reduce final target error. It also provides a button to move the robot towards the skin entry point and a button to set this point as the new reference of the robot's frame. This step is very important because every subpart works in this reference frame.

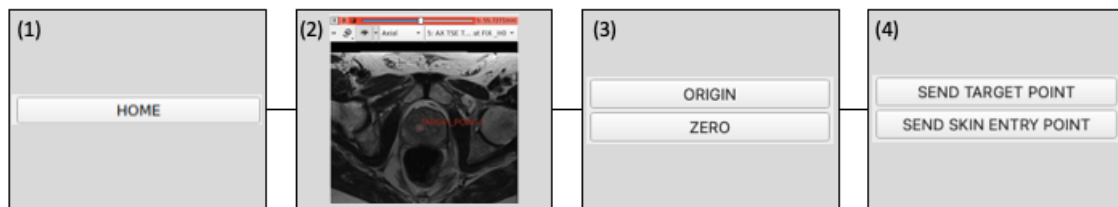


Figure 10: Steps for initialization: 1- HOME the robot: the guides travel along their axis before going back to beginning of axis. 2- Set target point on the prostate tumor by placing a fiducial over an MRI diagnostic image. 3- Press ORIGIN to move the robot to be aligned to that target point and ZERO the robot to set the skin entry point to be the origin of the robot's frame for coherence with the needle's frame. 4- Press button to publish target and skin entry point to ROS2 nodes.

Once the initialization phase is done, the closed-loop control can start and the interface is used as a feedback tool. First, it gives the clinician instructions on the depth and orientation that he should manually perform to correct deviation. This part of the control has not been implemented yet but sample values are published to emulate this function. Second, it provides the user with real-time position of the needle guide both with the exact values and a moving simulation of the robot (blue model parts). Finally, it also displays real-time 3D modeling of the needle shape. This UI communicates with ROS2 nodes in a bi-directional way using the ROS2-IGTLLink bridge. This bridge converts Slicer messages

types to ROS2 messages types and vice-versa. The added latency for the initialization part is not considered in the latency evaluation as no strict constraint of real-time is expected for initialization process.

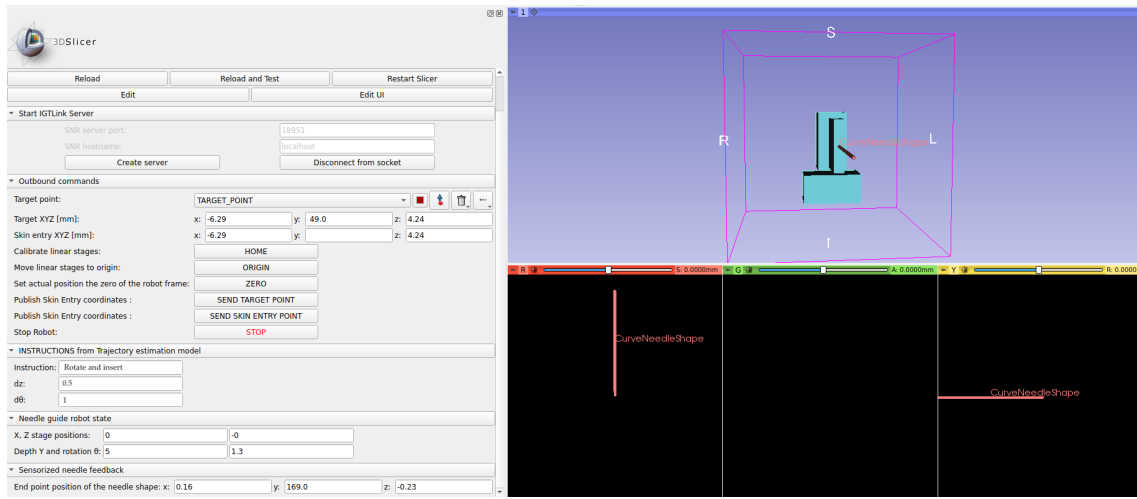


Figure 11: Sensorized Needle Module in *3D Slicer*

3 Validation experiments

3.1 Integration assessment in virtual, semi-virtual and real hardware setups

In order to validate integration, the latency of communication was assessed in different experimental setups. This first metric was defined as follows: the delay before the robot’s callback receives the moving instruction after pressing the keyboard (ie = the instruction asking for computing control position). These “start” and “end” times are visible on the sequential diagram Figure 5. The control approach being a semi “closed-loop” (alternate between base control by the robot and manual insertion by physician), the time taken by an information to be transferred across the nodes is measured as a one-way to its destination rather than as a round trip. Times are provided by the clock timer library of ROS2 (rclcpp:TimerBase) in ms with a precision of magnitude order of nanoseconds. The latency is thus the difference between these two times and expressed in ms (we keep 1 digit of precision even if more can be measured as values smaller than 0.1 ms have no impact on our hypothesis).

The first setup (A) is virtual only meaning that both the needle shape sensing and robot are simulated. The protocol consists in launching every node in simulation level, pressing the keyboard and recording the above mentioned start and end times. The pressing keyboard action is repeated 20 times in virtual setup. A first experiment was performed with 40 trials and the variance was of 2.1 ms so we estimated 20 trials to be sufficient for the other sets of experiment. For all the presented setups, our null hypothesis is that the latency obtained is inferior to the requirement limit estimated at 25 ms.

The second setup (B) is also virtual only but the needle nodes is launched on one computer whereas the robot and control algorithm nodes are launched on a second com-

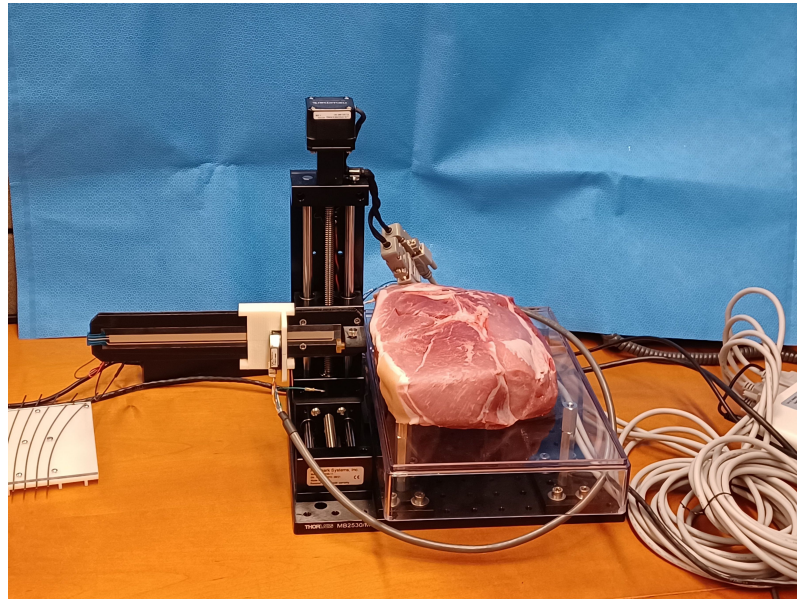


Figure 12: Picture of the experiment with the needle guide device and ex-vivo phantom.

puter. ROS2 nodes communicate together using Ethernet. The protocol is the same as for experiment A. The pressing keyboard action is repeated 20 times. This aims at testing if a setup where nodes run on separate machine is possible and assess flexibility of the integration.

The third and fourth setups for experiment are semi-virtual meaning that either the sensorized needle or the robot is real hardware, the other being simulation ((C) simulated needle/real robot, (D) real needle/ simulated robot). Again, 20 repetitions are measured for these two combination. This aims as testing if one can develop its physical hardware within the system without having access to the rest of the material.

The fifth setup (E) brings together all the hardware with the physical FBG sensorized needle and the robot guide. It can be seen in Figure 12. In this setup, the protocol requires a calibration phase before a “procedure” phase. The calibration phase for the robot relies on the Slicer module and follows the steps presented above in Figure 10. A calibration of the sensorized needle is also conducted using ROS2 node and a straight tube aligner. The “procedure” phase consisted in alternating manual insertion of approximately 1-1.5 cm with pressing the keyboard to achieve automated control. Again, 20 repetitions are measured to compute latency.

For each setup, we test the null hypothesis that the latency mean is not less than 25 ms with a significance level 0.05 with a one sample t-test. Our alternative hypothesis is that the latency mean is less than 25 ms with a significance level 0.05.

3.2 Preliminary evaluation of adaptive compensation strategy

The goal of this experiment is to have a first sense of the accuracy that can be achieved with the system with a simple proportional controller. The accuracy is evaluated by comparing the performance of the system to correct a straight insertion with an insertion where no-control is applied. As the target point is 0 in X and Z, the accuracy is defined as the

magnitude of the final tip position. The depth is not taken into account as it has no control strategy implemented yet. We thus use the full hardware setup with everything running in one computer (setup (E).) The used controller is a simplified proportional controller with a gain of 0.5 and a maximum control limit for lateral movement set to +/-0.5mm. The proportional gain has been tuned experimentally by increasing the gain until a control is observed. This tuning was performed for the different phantom used as it is dependent on the stiffness. At this stage of the project, there is no control acting on the insertion and rotation of the needle. The axial rotation was thus kept constant during insertion. Two different phantoms were used for this mock insertion experiment: an agar-gelatine phantom (2.5% dry-weight concentration) and an ex-vivo phantom of pork shoulder meat. Two insertions of approximately 100 mm were realized with and without control for gel and meat phantom. A target point of (0,0) was set as we align at the beginning the robot with the supposed target position. Again, the insertion consisted in inserting 1-1.5cm, then pressing keyboard to control the robot and repeat until full insertion (approximately 6 repetitions). The base position as well as the needle tip were recorded during the whole process. We only compute the mean of measurements in control and no control setups for different phantoms. No statistical analysis is performed because of the few number of trials. However, it is a sufficient number of trials to investigate our inference which is the capability of the system to perform multi-phase control and to measure performance.

4 Results

4.1 Latency results in virtual, semi-virtual and real hardware setups

The following Figure 13 displays boxplots of the latency obtained for the different explained setups.

We can see that the median value for the fully virtual setup running in one computer (A) is around 6 ms and is lower than any other configuration. A few outliers are however measured at 12 to 18 ms. The virtual setup running on separate computers (B) has a slightly increased median compared to setup (A). Setups with the real robot (C) and (E) have a wider range of values and a similar median around 8 ms. Lastly, setup (D) with the real FBG needle and virtual robot has a small range but highest median.

The p-values computed against the null hypothesis that the latency mean is more than 25 ms are presented in Table 2. Every value is below the significant criteria of 0.05 and thus we reject the null hypothesis for all the five tested setups. The mean value is statistically smaller than 25 ms for the virtual, semi-virtual and full hardware setups as well as when nodes run on two different computers and communicate via Ethernet.

Table 2: P-values obtained for setups (A) to (E) against the null hypothesis that the latency mean is not less than 25 ms the 95% confidence interval (CI).

Setup label	A	B	C	D	E
p-value *1.0e-13	0.0013	0.0000	0.0000	0.0002	0.1601
CI	[-∞;8.1]	[-∞;7.5]	[-∞;9.0]	[-∞;9.9]	[-∞;10.7]

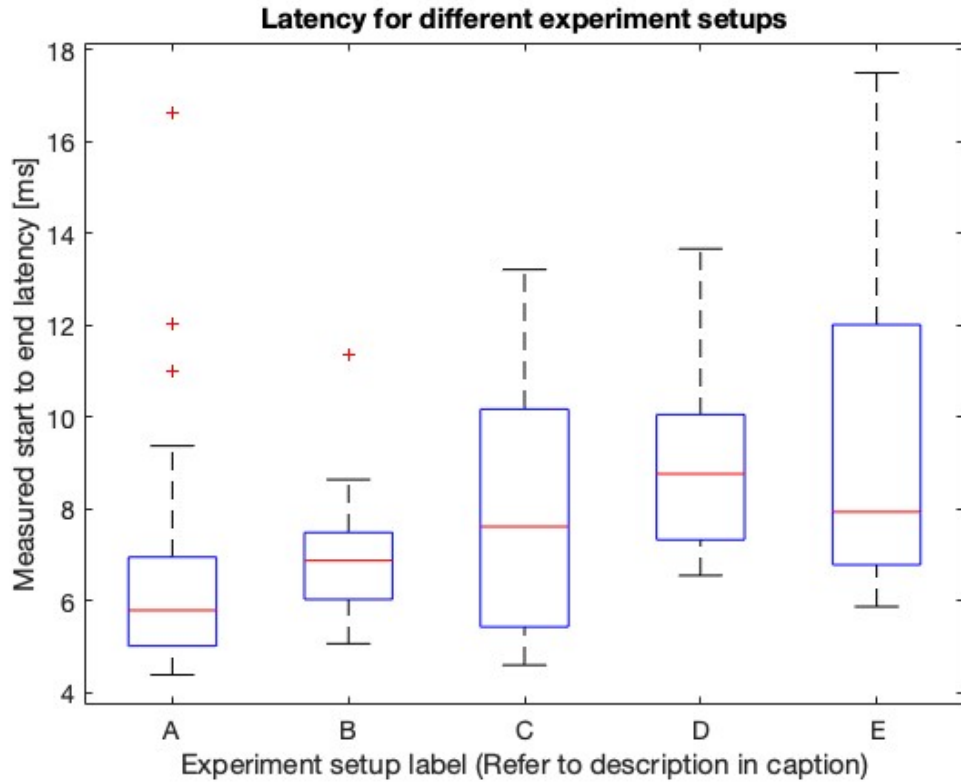


Figure 13: Boxplots of measured latency for (A) virtual-only simulation in one computer, (B) virtual-only simulation in two computer, (C) virtual needle/real robot, (D) real FBG needle/virtual robot, (E) real FBG needle/real robot

4.2 Preliminary accuracy results

On the following Figure 14, we plotted the end point position of the needle at the end of the insertion as well as the desired target point. In the gel phantom, the needle tip arrived closer to the target for the controlled insertions. The plot of the needle end points in the meat insertion show little difference between controlled and free insertion.

We estimated accuracy by computing the difference between the tip end position at the end of insertion with the target position:

$$\text{error} = \sqrt{(x_{\text{endtip}} - x_{\text{target}})^2 + (z_{\text{endtip}} - z_{\text{target}})^2} \quad (2)$$

With the target being zero, the error just becomes:

$$\text{error} = \sqrt{x_{\text{endtip}}^2 + z_{\text{endtip}}^2} \quad (3)$$

Table 3 presents the mean values of target error in mm for the two insertions performed in gelatine and ex-vivo phantom with the proportional controller. The right column presents the measured reference (ie. the mean of target errors measured for the two insertions realized in the same setup without any control applied.)

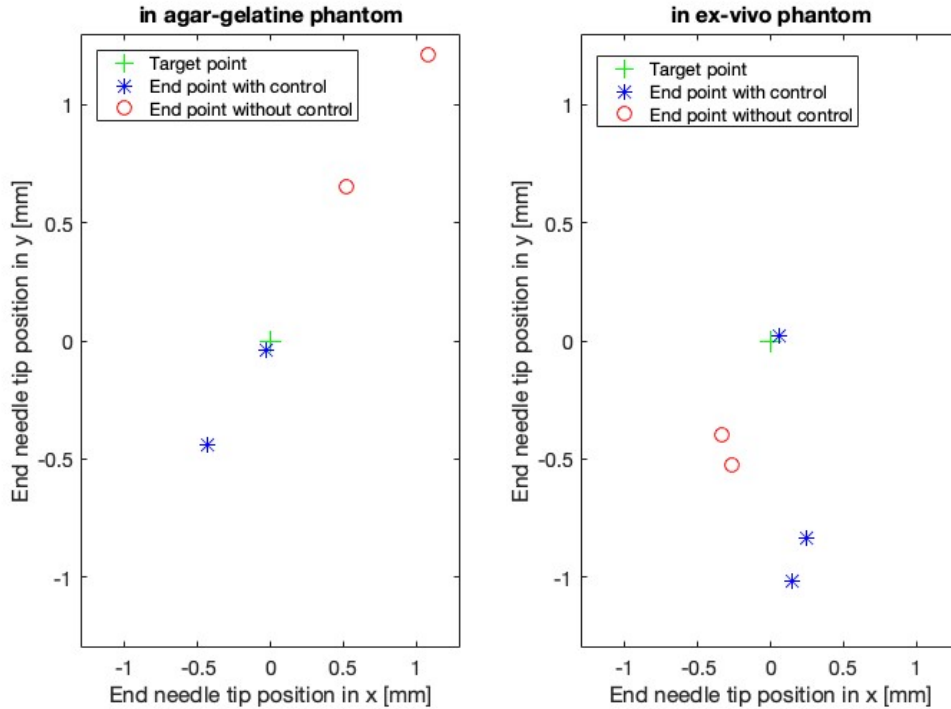


Figure 14: Needle tip position at the end of the insertion for a few trials for different parameters

Table 3: Target error measured in [mm]

	With control	Without control
Insertion in gel phantom	0.33	1.23
Insertion in ex-vivo phantom	0.65	0.56

We can see that in the gel phantom, the controlled insertion yields smaller end tip deviation than the no control experiment. The no control experiment represents here a comparative reference but cannot be defined as a ground truth as only two insertions have been performed. Regarding the ex-vivo trials, final deviation measured with and without control are still small (less than 1 mm). However, the final tip error is smaller for the trial that had no control.

5 Discussion

We have developed an integrated system that allows the first testing of a novel adaptive guide method for targeted prostate biopsy. This system architecture provides real-time exchange according to the defined requirement of 25 ms. This is achieved in different testing configurations including in ambivalent setups with a virtual part and a physical one. That enables developers to improve their subparts even without access to the fully physical system. Additionally, the integration has demonstrated real-time latency when the

robot and control run on one computer and the sensing needle node on another. Achieving good communication latency with nodes running on different computers can be useful for MRI clinical cases. Indeed, sometimes, an MRI-compatible machine stays inside the MRI room while the main processing of information is done outside. Also, if one part of the system requires high computational power; this could be the case with the final MPC implementation that relies on (9x9) Jacobian matrices ; being able to communicate between computers in real-time is primordial. A first assessment of the guide's performance showed that the control strategy is promising. It also shows that it needs further improvements and tests as in the ex-vivo setup, the controlled trajectory was less accurate than the free insertion. This can come from heterogeneity of the meat phantom but also inconsistent depth and speed of insertion between trials. Unlike most needle guides for prostate biopsy, the robot here allows to measure insertion depth and rotation while keeping a manual activation of the degrees of freedom. The integration provides the developers of the control strategy with measurements required to adjust the algorithm. Indeed, the fully-assembled device records 3 linear DOFs and one rotation of needle guide, the needle shape but also the computed Jacobian matrix required for the final MPC controller. This will enable testing and tuning of control strategy. Additionally, the sensorized needle's developers can now reproduce this system in their lab to improve their device which will allow future improvements of many clinical applications. More trials should be performed to assess the accuracy of this early-stage compensation strategy. An additional validation experiment that could be conducted is to measure the added latency of receiving MRI images.

6 Conclusion

In order to open new perspectives of MR-biopsy, we have developed an ROS2 integration system for needle guiding which incorporates a novel FBG sensing, a simple control algorithm and a user interface. Our simulation study showed that one can easily switch from virtual to semi-virtual to full physical implementation with real-time latency of communication. The pilot phantom study demonstrated that the needle guide control with novel sensing method allowed a positioning accuracy below 1 mm both in gel and ex-vivo phantom. However, the obtained accuracy did not always overcome the accuracy measured without control. This finding underlines that this new method combining automated and manual steering control is promising and encourages finer tuning and further experiments towards clinically-approved device.

C Project Conclusion

The main objective of this thesis was to realize the system integration of an adaptive needle guide strategy for targeted prostate biopsy interventions. This implied to design the architecture of the communication between the following subsystems: a sensorized needle, a control algorithm, a needle guide and a user interface. To this end, the first step taken was to create a joint Github project with a repository dedicated to system integration. Inside this repository, I created a Github controlled UML diagram of the different nodes and topics exchanged. It was updated by the collaborators and then served as a reference for the communication protocol. It allowed to detect heterogeneity in the topics names and types which would have otherwise been obstacles to integration and result in long times of debugging. Then, I created a ROS2 global launch file that facilitates the system's bring-up. Indeed, without such joint files, launching the system would require opening and sourcing each time eight shells. Additionally, I added simulation level argument to enable rapid switch between simulation and real hardware nodes. Switching between simulation and physical nodes without the parameters required looking for the name of the corresponding launch file for each subpart and re-starting the shells. With this new system configuration, one can easily run a quick test to verify communication before performing an experiment. Also, it allows easier debugging to identify which hardware might not be functioning by launching alternatively its simulation.

In order to bring these isolated developments to a concrete first experiment, a second step was to provide a physical needle guide. The robot's main body was assembled with a primary focus on X and Z automated movements. One faced challenge was to make the motor's controller work on Linux whereas the interface was designed for Windows. I thus dug into their Linux driver, updated it and integrated it to the stage control ROS2 node. To achieve the closed-loop control, the robot also has to provide measurements of depth and rotation. A technical challenge was to provide a sensing method that would not compromise the needle movement. A sliding carriage combining both linear and rotary encoder answers this need. An adapted needle holder was also designed and both pieces were 3D printed. The Arduino Uno board was chosen for the sensors integration. The Arduino IDE provides real-time measurements but a key question was how to integrate these measurements to the ROS2 system. Different solutions were explored and the satisfying one relies on the ROS Arduino library Rosserial as well as the bridge between ROS and ROS2.

The last piece to bring to the puzzle was the user interface. I made use of the OpenIGTLINK protocol as well as the ROS2-OpenIGTLINK library to integrate it to ROS2.

Finally, in order to validate integration, we measured the latency of the communication in different setups. The experiment consisted in performing iteration steps of the control strategy and record the start and end times of the information transfer. This was performed both in virtual, semi-virtual and full hardware setup and running in one or two machines. We performed a t-test statistical analysis against null hypothesis that the mean of the latencies is not inferior to 25 ms. The null hypothesis was rejected thus demonstrating that the communication between nodes in the integrated system will not limit the real-time requirement. Additionally, to benchtop the feasibility of the method, insertion trials were performed in agar and ex-vivo phantoms. The adaptive compensation achieved better target accuracy in the agar-gelatine phantom compared to insertion without control. Nonetheless, in the meat phantom, more similar to human-tissue, the difference between the controlled and free insertion were not very clear. Overall, this benchtop evaluation of adaptive compensation guide was successful in terms of integration and provided encouraging results. However, additional experiments are required to have a more precise reference of the no control insertion and to test with a high end control algorithm. On the following Figure 15 we can see the on-going work at John Hopkins University who reproduce the presented system in their Laboratory for Computational Sensing and Robotics (LCSR). They will use it to test and improve their device toward clinical tools that will enable improvements in the detection and treatment of PCa and other diseases.



Figure 15: Duplication of the setup developed in this study at John Hopkins University.

D Annexes

D.1 Arduino connections diagram

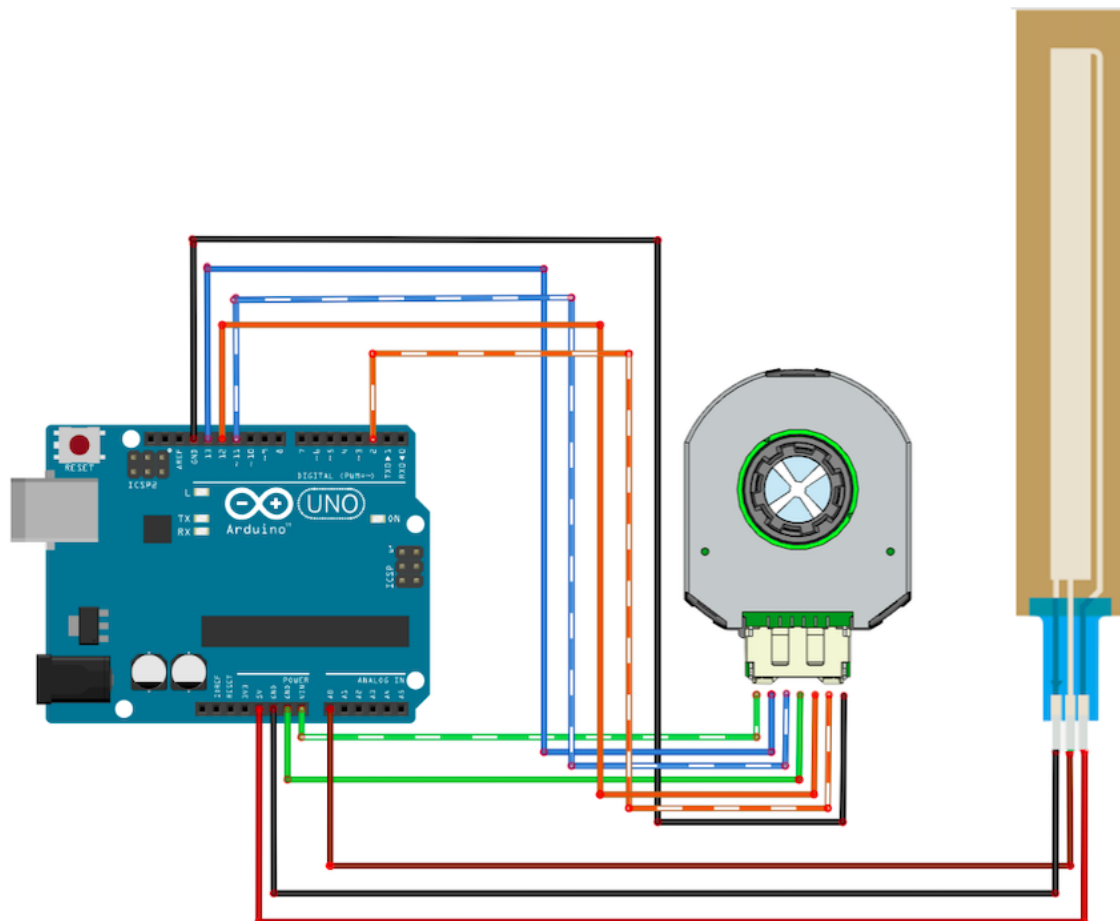


Figure 16: Circuit diagram to connect Arduino Uno board to CUI rotary encoder ATM222 and linear potentiometer *Softpot*

D.2 Hardware Assembly Guide

The following assembly guide is a combination of previous work realized in the lab with the novel designed pieces.

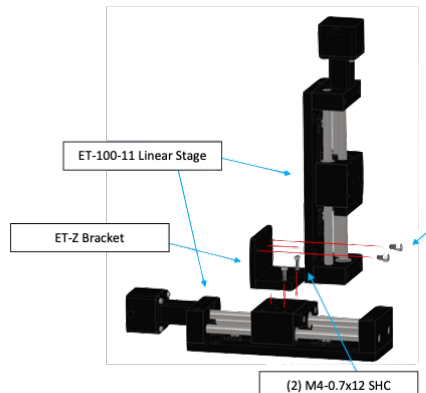


Figure 17: Linear stages assembly

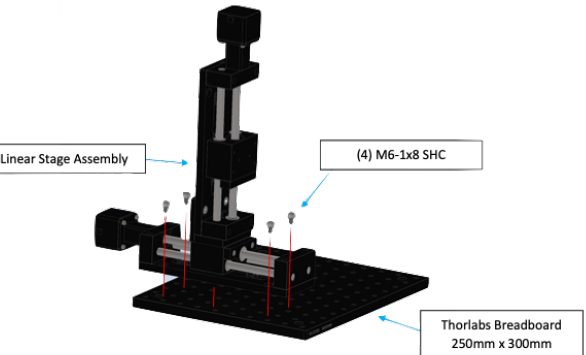


Figure 18: Base assembly

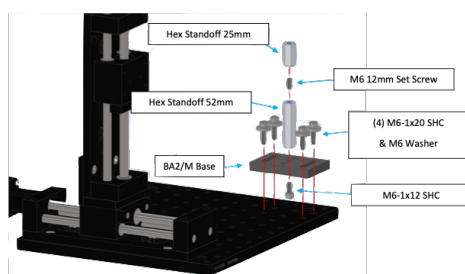


Figure 19: Supports assembly

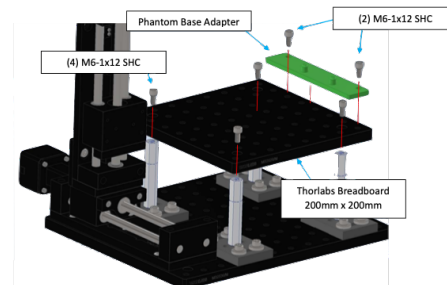


Figure 20: Top platform assembly

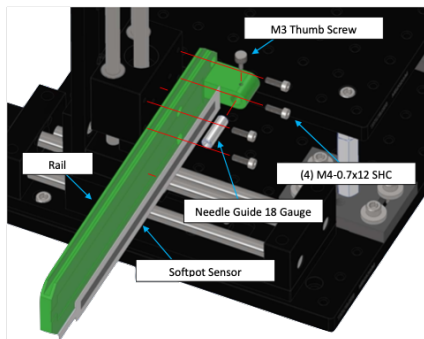


Figure 21: Linear potentiometer support assembly

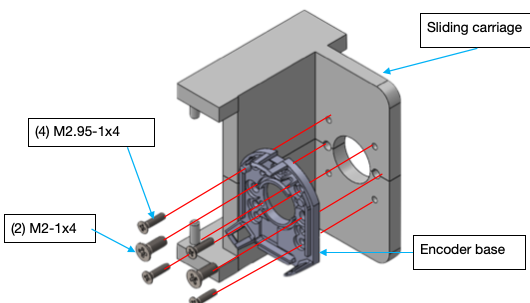


Figure 22: Sliding carriage and encoder base assembly

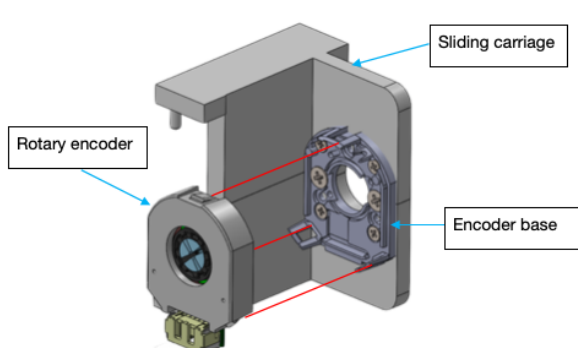


Figure 23: Rotary encoder and sliding carriage clipping

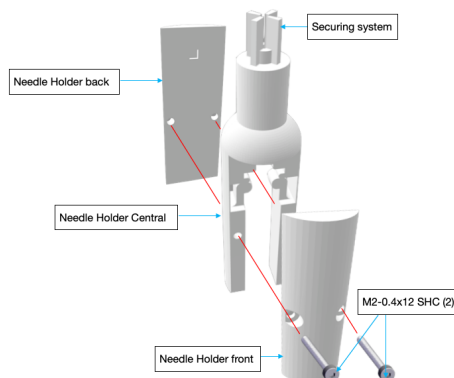


Figure 24: Needle holder assembly with cross-shaped end

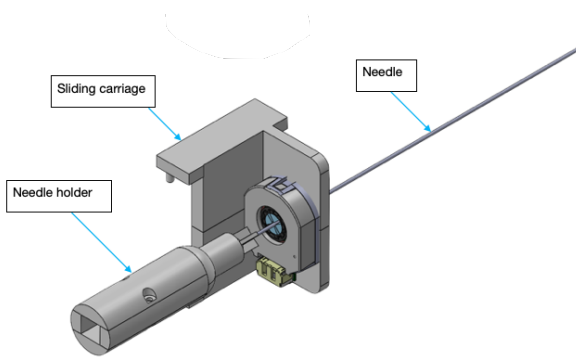


Figure 25: Needle holder mounted in the encoder

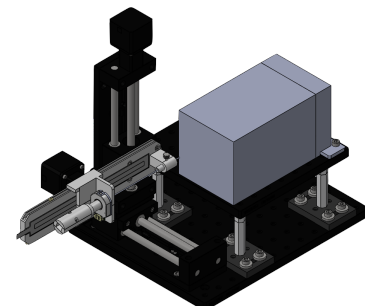


Figure 26: Final needle guide assembly

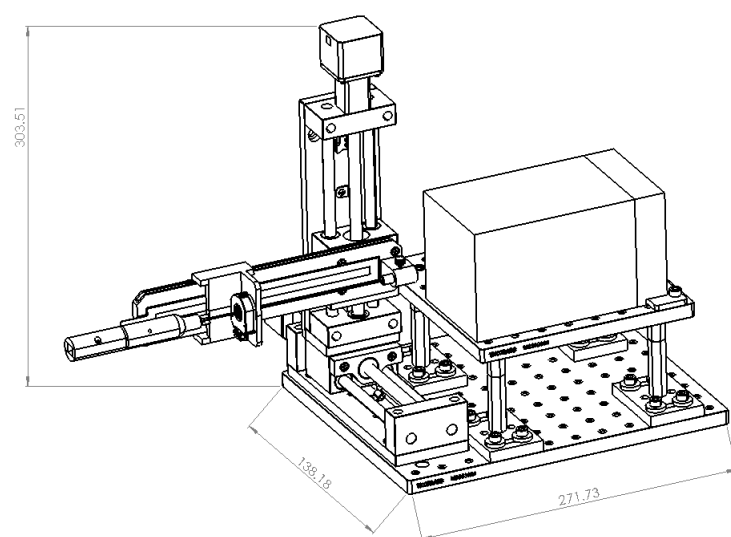


Figure 27: Final assembly's workspace

E Supplementary experiments

E.1 Intermediate virtual testing

In order to ensure that the subsystems function together as a system, an intermediate virtual test has been performed. It consisted in verifying the implementation of the system diagram and communication between the collaborators' nodes. The simulation of the robot's functionalities was achieved using the previously developed Gazebo simulation as well as the newly implemented sensors' simulation. As explained, both depth and rotation sensors have been simulated using a simple publisher that increases sample values. These values range from -150 to 0 mm for depth and from 0 to π rad for the rotation. Different test conditions and metrics were measured to assess the success of the testing:

- **Test I Condition:** The simulated needle guide robot publishes 100 X,Y,Z, θ sample values. **Metric I-a and I-b:** the needle shape publisher receives the values and trajectory control algorithm receives the value.
- **Test II Condition:** In response to Test I condition, the needle shape publisher publishes 100 pre-set values of “Strain Data” all showing straight needle shape. **Metric II-a:** the trajectory control algorithm node receives the values.
- **Test III Condition:** In response to Test II condition, the trajectory control algorithm node sends $xi=0$, $zi=0$ to the needle guide. **Metric III-a and III-b:** the simulated needle guide produces xi , zi = and issues new position parameters.

This early testing was successful for every listed metric. We ensured an easy-to-launch system and fluid communication. This intermediate virtual testing served as a basis for each collaborator to test the whole system on its own. Once system integration is verified for simulation, it becomes easier for each party to build new blocks and integrate them to the already approved communication organization.

E.2 Testing in different gel phantom stiffness

An initial set of five insertions had been performed in a low-stiffness gelatine phantom. The same protocol was followed. We first started with setting a (0,0) target point using the Slicer module. Then, we alternated 1-1.5 cm insertion with a keyboard press to generate automated control. The control was performed with a controller gain of 0.1 for two insertions and 0.5 for three insertions. The same FBG sensorized needle from JHU was used, thus an 18-gauge needle. The setup can be seen on Figure 28. Over every insertion, the robot did not move meaning that no control command was provided. We can explain this observation with the fact that an 18-gauge does not undergo any deviation in a gelatine phantom of small stiffness. This was then verified by looking at the measures provided by the shape sensing. Thus, for future experiments, one should not use a gelatine phantom of small stiffness with such needle diameter.

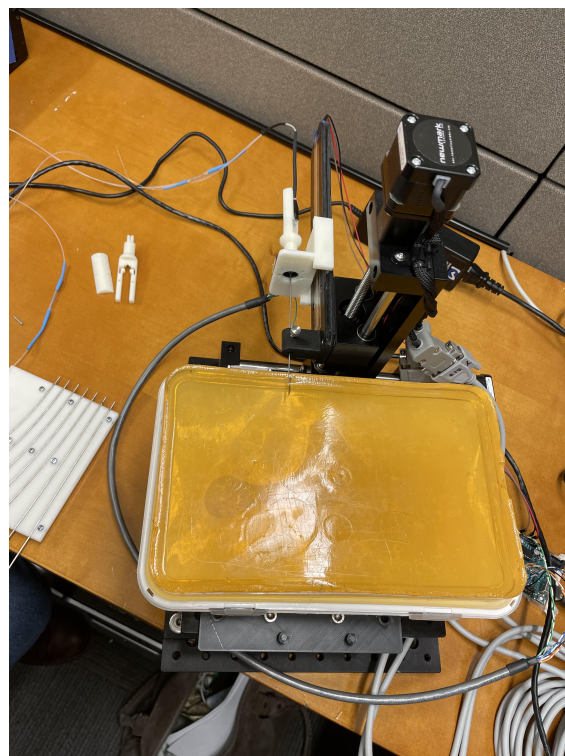


Figure 28: Insertion performed in a gelatine phantom.

E.3 Evaluation of the needle guide's settling time

An often critical component of surgical interventions is the time of the operation. Indeed, with an increased time comes increased infectious risks and additional costs. Also, it is more difficult for the physician's to stay focus and limit human errors in long-time interventions. Thus, a key point of clinically-approved devices is the procedure time. With this innovative semi-closed loop control, the two main parameters of the intervention time are the rapidity of the physician and the rapidity of the robot to achieve a goal. The settling time of the robot is thus the time it takes for the robot to move to the received position goal. An internal study defined that a range between 0.5 and 1 s is acceptable for the robot. In order to test this hypothesis, we compute the settling time for 10 insertion steps both in the agar-gelatine and ex-vivo phantom. The mean values obtained for both setups are provided in Table 4. We also run a t-test against the null hypothesis that the settling times are above 1s. The obtained p-values with a 95% confidence intervals are also provided in Table 4.

Table 4: Mean settling times and p-values for different phantom experiments.

Phantom	Settling time [ms]	p-value
Agar-gelatine phantom	0.2533	1.4180e-09
Ex-vivo phantom	0.3198	2.0430e-06

According to the results of the t-test, we can say that settling times are below the mean value of 1s in both phantoms. The settling time is bigger for the ex-vivo phantom which might be explained by a higher deviation due to tissue density and thus bigger correction required.

E.4 Integration test with another sensorized needle method

- Hypothesis

In order to challenge the integration strategy adopted here and demonstrate its repeatability, we tested the system with another sensorized needle technique. The other sensorized needle makes use of the commercially-available *Aurora* sensor. The Aurora sensor is an electromagnetic tracking solution for precise interventional applications. Aurora delivers real-time sensing with a typical throughput similar to the FBG needles. Thus, following our previous hypothesis. We test the null hypothesis that the mean latency measured with the Aurora needle is not below 25 ms.

- Validation Method

The same experiment than for the FBG needle was performed. An agar-gelatine phantom of 2.5% dry-weight concentration was used for the insertion. An image of the setup in provided in Figure 29 A calibration was required before the start of the experiment as, in contrary to the FBG needle, the Aurora needle provides sensing in the Aurora frame rather than in the robot frame. To perform calibration, we used a template with 5 mm distance reference points. We measured with Aurora the value of five points of known position on the template. Then, the transform matrix between the template and the Aurora sensor is computed and saved. We can then perform the experiment knowing that everything works in the robot's frame. Apart from this additional calibration step, the

protocol is the same than for the FBG needle. Indeed, by complying to the topics' names and types defined in the configuration diagram, one can easily test its subpart within a fully integrated system. We then realized 20 insertion steps of . Then, we compute the p-values against the aforementioned null hypothesis with a 95% confidence interval. The second hypothesis is that the setup can control the Aurora needle and measure accuracy.

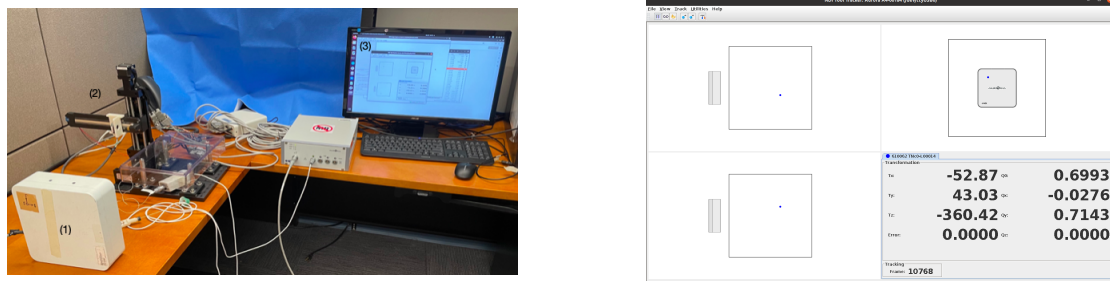


Figure 29: Experimental setup using (1) the Aurora sensor (2) the developed needle guide robot, and (3) the developed 3DSlicer interface and Aurora Interface. On the right image is the Aurora readings with the needle tip position in blue.

- Results

The computed p-values against the null hypothesis that the latency obtained with a different sensing needle is not below 25 ms are provided in Table 5.

Table 5: Mean latencies and p-values for different phantom experiments.

Phantom	Latency mean [ms]	p-value
Agar-gelatine phantom	9.2	1.0e-13 * 0.000

We could not perform the accuracy assessment because as soon as the needle was inserted into the phantom, Aurora device kept loosing track of the needle tip position.

- Discussion

With this new sensorized needle but with the same configuration, we were able to perform integration without many adjustments. The communication latency was again validated against the upper value of 25 ms. We were able to achieve the closed-loop control: when Aurora measured a deviation, the robot moved. However, because of instability of the sensors readings, we could not assess the accuracy of the method. This instability probably comes from the presence of multiple metallic parts of the needle guide that interfere with Aurora magnetic field. For further experiments with this needle sensing, we should modify the robot's body by changing platforms to plastic ones for instance.

REFERENCES

- [1] Prashanth Rawla. "Epidemiology of Prostate Cancer". eng. In: *World journal of oncology* 10.2 (Apr. 2019), pp. 63–89. ISSN: 1920-454X. DOI: 10.14740/wjon1191.
- [2] Henrik Grönberg. "Prostate cancer epidemiology". In: *The Lancet* 361.9360 (2003), pp. 859–864. ISSN: 0140-6736. DOI: [https://doi.org/10.1016/S0140-6736\(03\)12713-4](https://doi.org/10.1016/S0140-6736(03)12713-4).
- [3] James A Talcott et al. "Time course and predictors of symptoms after primary prostate cancer therapy". In: *Journal of Clinical Oncology* 21.21 (2003), pp. 3979–3986. ISSN: 0732-183X.
- [4] William J. Catalona et al. "Measurement of Prostate-Specific Antigen in Serum as a Screening Test for Prostate Cancer". In: *New England Journal of Medicine* 324.17 (Apr. 1991), pp. 1156–1161. ISSN: 0028-4793. DOI: 10.1056/NEJM199104253241702.
- [5] Michael E. Chua et al. "2013 Annual National Digital Rectal Exam Day: impact on prostate health awareness and disease detection". In: *Prostate International* 2.1 (Mar. 2014), pp. 31–36. ISSN: 2287-8882. DOI: 10.12954/PI.13039.
- [6] Hans Lilja, David Ulmert, and Andrew J. Vickers. "Prostate-specific antigen and prostate cancer: prediction, detection and monitoring". In: *Nature Reviews Cancer* 8.4 (Apr. 2008), pp. 268–278. ISSN: 1474-1768. DOI: 10.1038/nrc2351.
- [7] Robert C. Flanigan et al. "Accuracy of Digital Rectal Examination and Transrectal Ultrasonography in Localizing Prostate Cancer". In: *The Journal of Urology* 152.5, Part 1 (1994), pp. 1506–1509. ISSN: 0022-5347. DOI: [https://doi.org/10.1016/S0022-5347\(17\)32457-6](https://doi.org/10.1016/S0022-5347(17)32457-6).
- [8] Konstantinos Devetzis, Francesca Kum, and Richard Popert. "Recent Advances in Systematic and Targeted Prostate Biopsies". eng. In: *Research and reports in urology* 13 (Nov. 2021), pp. 799–809. ISSN: 2253-2447. DOI: 10.2147/RRU.S291963.
- [9] Magne Dimmen et al. "Transperineal prostate biopsy detects significant cancer in patients with elevated prostate-specific antigen (PSA) levels and previous negative transrectal biopsies:" en. In: *BJU International* 110.2b (July 2012), E69–E75. ISSN: 14644096. DOI: 10.1111/j.1464-410X.2011.10759.x.
- [10] Misop Han et al. "Geometric Evaluation of Systematic Transrectal Ultrasound Guided Prostate Biopsy". In: *Journal of Urology* 188.6 (2012), pp. 2404–2409. DOI: 10.1016/j.juro.2012.07.107.
- [11] Hashim Uddin Ahmed et al. "The PROMIS study: A paired-cohort, blinded confirmatory study evaluating the accuracy of multi-parametric MRI and TRUS biopsy in men with an elevated PSA." In: *Journal of Clinical Oncology* 34.15_suppl (May 2016), pp. 5000–5000. ISSN: 0732-183X. DOI: 10.1200/JCO.2016.34.15_suppl.5000.
- [12] Hashim U Ahmed, Ahmed El-Shater Bosaily, and Louise C Brown. "Diagnostic accuracy of multi-parametric MRI and TRUS biopsy in prostate cancer (PROMIS): a paired validating confirmatory study". In: *The Lancet* 389.10071 (Feb. 2017), pp. 815–822. ISSN: 01406736. DOI: 10.1016/S0140-6736(16)32401-1.
- [13] D. D'Agostino et al. "In-Bore" MRI-Guided Prostate Biopsy for Prostate Cancer Diagnosis: Results from 140 Consecutive Patients". In: *Current Urology* 14.1 (2020). ISSN: 1661-7649. DOI: 10.1159/000499264.

REFERENCES

- [14] Philippe Puech et al. "Prostate Cancer Diagnosis: Multiparametric MR-targeted Biopsy with Cognitive and Transrectal US–MR Fusion Guidance versus Systematic Biopsy—Prospective Multicenter Study". In: *Radiology* 268.2 (Aug. 2013), pp. 461–469. ISSN: 0033-8419, 1527-1315. DOI: 10.1148/radiol.13121501.
- [15] David Ka-Wai Leung et al. "Role of pre-biopsy multiparametric MRI in prostate cancer diagnosis: Evidence from the literature". In: *Turkish journal of urology* 47.Supp. 1 (Feb. 2021), S65–S70. ISSN: 2149-3235. DOI: 10.5152/tud.2020.20360.
- [16] Veeru Kasivisvanathan et al. "MRI-Targeted or Standard Biopsy for Prostate-Cancer Diagnosis". In: *New England Journal of Medicine* 378.19 (May 2018). Publisher: Massachusetts Medical Society, pp. 1767–1777. ISSN: 0028-4793. DOI: 10.1056/NEJMoa1801993.
- [17] Gaurie Tilak et al. "3T MR-guided in-bore transperineal prostate biopsy: A comparison of robotic and manual needle-guidance templates: Robotic Template for MRI-Guided Biopsy". In: *Journal of Magnetic Resonance Imaging* 42.1 (July 2015), pp. 63–71. ISSN: 10531807. DOI: 10.1002/jmri.24770.
- [18] Christopher Warlick et al. "Beyond transrectal ultrasound-guided prostate biopsies: available techniques and approaches". In: *World Journal of Urology* 37 (Mar. 2019). DOI: 10.1007/s00345-018-2374-8.
- [19] Mark S. Litwin and Hung-Jui Tan. "The Diagnosis and Treatment of Prostate Cancer: A Review". In: *JAMA* 317.24 (June 2017), pp. 2532–2542. ISSN: 0098-7484. DOI: 10.1001/jama.2017.7248.
- [20] Matthew A Uhlman et al. "Tumor volume, tumor percentage involvement, or prostate volume: which is predictive of prostate-specific antigen recurrence?" In: *Urology* 75.2 (Feb. 2010), pp. 460–466. ISSN: 1527-9995. DOI: 10.1016/j.urology.2009.06.059.
- [21] Cevahir Özer and Bermal Hasbay. "Concordance between needle biopsy and radical prostatectomy specimens in prostatic carcinoma". In: *Acta Oncologica Turcica* 53.3 (2020), pp. 396–401. DOI: 10.5505/aot.2020.36459. URL: <https://dx.doi.org/10.5505/aot.2020.36459> (visited on 01/02/2020).
- [22] Jonas Hugosson, Johan Stranne, and Sigrid V. Carlsson. "Radical retropubic prostatectomy: A review of outcomes and side-effects". In: *Acta Oncologica* 50.sup1 (June 2011), pp. 92–97. ISSN: 0284-186X. DOI: 10.3109/0284186X.2010.535848.
- [23] Youngmee Kim, Joseph A. Roscoe, and Gary R. Morrow. "The effects of information and negative affect on severity of side effects from radiation therapy for prostate cancer". In: *Supportive Care in Cancer* 10.5 (July 2002), pp. 416–421. ISSN: 1433-7339. DOI: 10.1007/s00520-002-0359-y.
- [24] Javier Romero-Otero et al. "Active surveillance for prostate cancer". In: *International Journal of Urology* 23.3 (Mar. 2016), pp. 211–218. ISSN: 09198172. DOI: 10.1111/iju.13016.
- [25] Thomas J Polascik and Vladimir Mouraviev. "Focal therapy for prostate cancer". In: *Current Opinion in Urology* 18.3 (2008). ISSN: 0963-0643. URL: https://journals.lww.com/co-urology/Fulltext/2008/05000/Focal_therapy_for_prostate_cancer.4.aspx.
- [26] S. Song et al. "Development and Preliminary Evaluation of a Motorized Needle Guide Template for MRI-Guided Targeted Prostate Biopsy". In: *IEEE Transactions on Biomedical Engineering* 60.11 (Nov. 2013), pp. 3019–3027. ISSN: 1558-2531. DOI: 10.1109/TBME.2013.2240301.

- [27] Bogdan Maris et al. “Pre-Clinical Validation of a Semi-Autonomous Robot for Transperineal Prostate Biopsy”. In: *IEEE Transactions on Medical Robotics and Bionics* (2022), pp. 1–1. ISSN: 2576-3202. DOI: 10.1109/TMRB.2022.3159737.
- [28] R. J. Roesthuis et al. “Three-Dimensional Needle Shape Reconstruction Using an Array of Fiber Bragg Grating Sensors”. In: *IEEE/ASME Transactions on Mechatronics* 19.4 (Aug. 2014), pp. 1115–1126. ISSN: 1941-014X. DOI: 10.1109/TMECH.2013.2269836.
- [29] Junwei He et al. “Comparisons of efficacy and complications between transrectal and transperineal prostate biopsy with or without antibiotic prophylaxis”. In: *Urologic Oncology: Seminars and Original Investigations* (Feb. 2022). ISSN: 1078-1439. DOI: 10.1016/j.urolonc.2022.01.004.
- [30] Andrian Andrian et al. “Case Report: High-grade anterior prostate cancer previously undetected by transrectal biopsy, diagnosed with MRI-US fusion transperineal robotic prostate biopsy”. In: *F1000Research* 11 (Feb. 2022), p. 247. ISSN: 2046-1402. DOI: 10.12688/f1000research.109546.1.
- [31] Emilie Lecornet et al. “The Accuracy of Different Biopsy Strategies for the Detection of Clinically Important Prostate Cancer: A Computer Simulation”. en. In: *Journal of Urology* 188.3 (Sept. 2012), pp. 974–980. ISSN: 0022-5347, 1527-3792. DOI: 10.1016/j.juro.2012.04.104. URL: <http://www.jurology.com/doi/10.1016/j.juro.2012.04.104> (visited on 04/01/2022).
- [32] Graham C Goodwin, Stefan F Graebe, and Mario E. Salgado. *Control system design*. Upper Saddle River, N.J., Prentice Hall., 2001.
- [33] <https://github.com/SmartNeedle>.
- [34] G. S. Fischer et al. “MRI-Compatible Pneumatic Robot for Transperineal Prostate Needle Placement”. In: *IEEE/ASME Transactions on Mechatronics* 13.3 (June 2008), pp. 295–305. ISSN: 1941-014X. DOI: 10.1109/TMECH.2008.924044.
- [35] https://github.com/rosl2/rosl1_bridge.
- [36] https://github.com/openigtlink/rosl2_igtl_bridge.

List of Figures

1	Interventional setup of a 3T MR-guided in-bore transperineal prostate biopsy 2014, Gaurie Tilak Bs et Al. It shows the (1) stirrups placed on (2) the patient table, (3) the robotic needle-guidance template, and (4) an abdominal surface coil, inside the MRI [17].	4
2	MR-fusion biopsy interface. On the top is shown the real-time ultrasound image acquired during operation. On the bottom is shown the pre-intervention MRI diagnostic image which locates the suspicious targeted region. This region is mapped onto the live US image. [18]	4
3	Architecture diagram of closed-loop control system. In green, the parts I was responsible for: the needle guide and GUI interface. In blue, the block diagram for the MPC strategy elaborated by a team at SNR lab. Lastly, the sensorized needle developed by collaborators at John Hopkins University (JHU).	6
4	Proposed adaptive control strategy: 1. Alignment of robot with target point. 2. When elastic skin contact happens, 3. the correcting solution is to move the base of the needle guide using the two automated axis of the robot. 4. In case of tissue-needle deviation inside the body, instructions will be sent to the physician to rotate the needle so that the position of the tip cancels the observed deviation.	7
5	Sequence diagram of main nodes publishers and subscribers. Notes indicate the beginning and end publisher/subscriber used to define latency. Grey boxes highlight the different repositories.	12
6	Kinematic diagram of the needle guide.	13
7	Equation of the needle base position.	13
8	CAD drawing of the sliding carriage, with the encoder based attached, and the rotary encoder.	16
9	Picture of the 3D printed needle holder. From left to right: the bottom cap, a central part adapted to different needle hubs and a top cap. The needle is secured to the sleeve adapter of CUI design thanks to its cross-end shape.	17
10	Steps for initialization: 1- HOME the robot: the guides travel along their axis before going back to beginning of axis. 2- Set target point on the prostate tumor by placing a fiducial over an MRI diagnostic image. 3- Press ORIGIN to move the robot to be aligned to that target point and ZERO the robot to set the skin entry point to be the origin of the robot's frame for coherence with the needle's frame. 4- Press button to publish target and skin entry point to ROS2 nodes.	17
11	Sensorized Needle Module in <i>3D Slicer</i>	18
12	Picture of the experiment with the needle guide device and ex-vivo phantom.	19
13	Boxplots of measured latency for (A) virtual-only simulation in one computer, (B) virtual-only simulation in two computer, (C) virtual needle/real robot, (D) real FBG needle/virtual robot, (E) real FBG needle/real robot	21
14	Needle tip position at the end of the insertion for a few trials for different parameters	22
15	Duplication of the setup developed in this study at John Hopkins University.	25
16	Circuit diagram to connect Arduino Uno board to CUI rotary encoder <i>ATM222</i> and linear potentiometer <i>Softpot</i>	26
17	Linear stages assembly	27

18	Base assembly	27
19	Supports assembly	27
20	Top platform assembly	27
21	Linear potentiometer support assembly	27
22	Sliding carriage and encoder base assembly	27
23	Rotary encoder and sliding carriage clipping	28
24	Needle holder assembly with cross-shaped end	28
25	Needle holder mounted in the encoder	28
26	Final needle guide assembly	28
27	Final assembly's workspace	28
28	Insertion performed in a gelatine phantom.	30
29	Experimental setup using (1) the Aurora sensor (2) the developed needle guide robot, and (3) the developed 3DSlicer interface and Aurora Interface. On the right image is the Aurora readings with the needle tip position in blue.	32

List of Tables

1	Design specifications of the proposed needle guide, provided by the chosen hardware.	14
2	P-values obtained for setups (A) to (E) against the null hypothesis that the latency mean is not less than 25 ms the 95% confidence interval (CI).	20
3	Target error measured in [mm]	22
4	Mean settling times and p-values for different phantom experiments.	31
5	Mean latencies and p-values for different phantom experiments.	32